Power Efficiency of the Rotational-to-Linear Infinitely Variable Cobotic Transmission

Eric L. Faulring, J. Edward Colgate, and Michael A. Peshkin

Abstract— **Cobots are a class of robots that use infinitely variable transmissions to develop high fidelity programmable constraint surfaces. Cobots consume very little electrical power even when resisting high forces, and their transmissions are highly power efficient across a broad range of transmission ratios. We have recently introduced the Cobotic Hand Controller, a haptic display that illustrates the high dynamic range and low power consumption achievable by cobots. In this paper we present models of the rotational-to-linear rolling contact transmissions utilized in the Cobotic Hand Controller. We compare their efficiency to fixed ratio gear-trains. We also compare the overall power efficiency of the cobotic architecture to the power efficiency of a conventional electro-mechanical actuation scheme, for both constant and dynamic power flows. The cobotic architecture is shown to be more efficient at frequencies and power levels characteristic of voluntary human motions.**

I. INTRODUCTION

COBOTIC devices control the relative velocities of their links by modulating infinitely variable transmissions (IVTs) with small steering actuators [1]. Cobotic IVTs have been developed to relate two translational velocities, two rotational velocities, or a rotational velocity to a translational velocity, and have been utilized in a variety of haptic[1] devices [2], [3], [4], [5].

Cobotic technology provides a highly power and weight efficient transmission architecture that can have minimal dissipation and trivial dynamics. Gear trains, timing belt transmissions, hydraulic and pneumatic systems as well as cable systems all have dissipative losses that result in heat and noise generation. In addition, stiction, friction, compliance and backlash in these transmissions add highly nonlinear dynamics to mechanisms. Cobotic transmissions utilizing bearing quality steel components in dry-friction rolling-contact have none of these nonlinearities. The attractive properties of transmissions based on rolling constraints led to the adoption of such mechanisms outside of the haptics community long before their use for cobots. Dry-friction rolling contact IVTs and/or traction-fluid mediated IVTs have been analyzed by [6], [7], [8], [9], [10], [11], [12], [13].

[1]Haptic displays convey touch and kinesthetic feedback to a human operator by dynamically varying the relationship between motion and force, often in the form of virtual constraint surfaces. Haptic displays are used to interact with computer aided design models, flight simulators, telerobotic surgery, micro/nano-manipulation, undersea salvage, as well as maintenance of nuclear plants and other hazardous environments.

Using an infinitely variable cobotic transmission can eliminate the need to make compromises on flow and effort, which are inherent in choosing a fixed transmission ratio, and also allow the actuators to be operated at an efficient speed nearly all of the time. In addition, the cobotic architecture allows for the ability to both clutch or decouple joints without any additional actuators beyond the low-power steering actuator for each IVT. Cobotic transmissions have a built in safety feature as well. Since they rely on frictional contacts to transmit power, the preload force at these contacts can be set to slip when a certain force or link acceleration is exceeded.

In this paper we show analytically and experimentally that the cobotic rolling contact transmission element is as efficient as gears. We also demonstrate that the entire cobotic system, including bearings and actuators and supporting structures, is as efficient or more so than a conventional fixed-ratio electro-mechanical system for steady-state and dynamic scenarios. The scenarios considered are at power and frequency of motion scales characteristic of human operation. In order to accurately predict the power efficiency of a cobotic transmission, all dissipative losses must be characterized and incorporated into a model of power flow in the transmission. The dissipative losses of dry-friction rolling contact have long been studied in the railroad and automotive industry [14], [15]. Dry-friction cobotic IVT mechanics have been studied by [12], [16], [17], [18]. These studies elucidate the impact of material properties and geometry on lateral and longitudinal elastic deformation based creeps, rolling friction, and steering friction.[2] [19] presents a model and [20], [21] and [22] present experimental data that isolate kinematic-creep (a rigid body sliding contact dissipative effect termed complete-slip in [14] and [15]) in the spherical IVT. They characterize the impedance across a spherical IVT from input drive-shaft to output drive-shaft. Understanding how design parameters such as component shapes and dimensions, material choices and loading conditions affect compliance and dissipation, leads to both mechanical and control choices to maximize the system's dynamic range, as well as improve power efficiency.

In Section II we introduce the rotational-to-linear infinitely variable transmission. In Section III we model the lateral creep and rolling losses found in the transmission element. Rolling friction (due inelastic properties of rolling bodies) and lateral creep (due to elastic deformation properties of rolling bodies) are present, and determine most of our de-

[2]We take *lateral* to mean transverse to the rolling direction and *longitudinal* to mean tangent to the rolling direction.

vice's power dissipation and impedance properties.[3] In Section IV we use this model to predict efficiency of the cobotic transmission across a wide range of operating conditions. We compare these results with experimental data from the Cobotic Hand Controller, and with conventional gear-train efficiencies. In Section V we develop complete bond graph descriptions of cobotic and conventional systems.[4] Note the delineation between *transmission* and *system*. By *transmission* we mean just a rolling contact reduction element, or a pair of gears. By *system* we mean all components of an architecture, including motors, guideways and transmissions. In Section VI we provide a comparison of the power efficiency of a cobotic system with that of a conventional electro-mechanical system for both constant power throughput and sinusoidal power throughput across a range of frequencies. Finally, in Section VII we conclude and make suggestions for future work.

II. BACKGROUND

A. The Lossless Rotational-to-Linear Transmission

The Cobotic Hand Controller haptic display introduced in [24] utilizes rotational-to-linear infinitely variable transmissions. Operation of these transmissions is depicted in Figure 1 while notation is given in Figure 2. The transmissions consist of a steered wheel whose steering angle, ϕ, relates the linear velocity, $\dot{l}$, of a prismatic link to the rotational velocity of a cylinder, ω. An assembly not shown in Figure 1 links the IVT wheel to the prismatic link (see [24] for a detailed depiction). The wheel is pressed against the cylinder with preload force, P, and a coefficient of friction, μ, describes the resistance to lateral loads on the wheel while rolling. A bond graph representation of this transmission is depicted in Figure 2. This graph yields Equation 1 which relates the flows for the rotational-to-linear transmission.

$$\frac{\dot{l}}{\omega} = -R \tan(\phi) \tag{1}$$

Here we have neglected flow losses such as lateral creep, described in later sections of this paper. The bond graph also yields Equation 2, which relates the efforts of the rotational-to-linear transmission.

$$\frac{f_l}{\tau} = -\frac{1}{R \tan(\phi)} \tag{2}$$

Here we have neglected effort losses such as rolling losses due to friction in the transmission and the IVT wheel axle bearings which are described in later sections of this paper. When the wheel is steered such that its rolling axis is parallel to the cylinder's, ($\phi = 0$), zero flow of the prismatic link is requested. If the wheel is steered in either direction from $\phi = 0$, flow of the prismatic link between $\pm$ infinity can be requested. In practice, wheel slip limits this range. Turning the wheel to $\phi = 0$ locks the prismatic link, and turning it to $\phi = \pi/2$ completely decouples the actuator from the cylinder's velocity, although the cylinder would then be unable to turn.

---

[3]Kinematic-creep is not present in the rotational-to-linear IVT analyzed here, as the rolling elements of our geometry do not sustain significant tractive loads.

[4]Karnopp et al. provide an excellent review of bond graph notation [23].
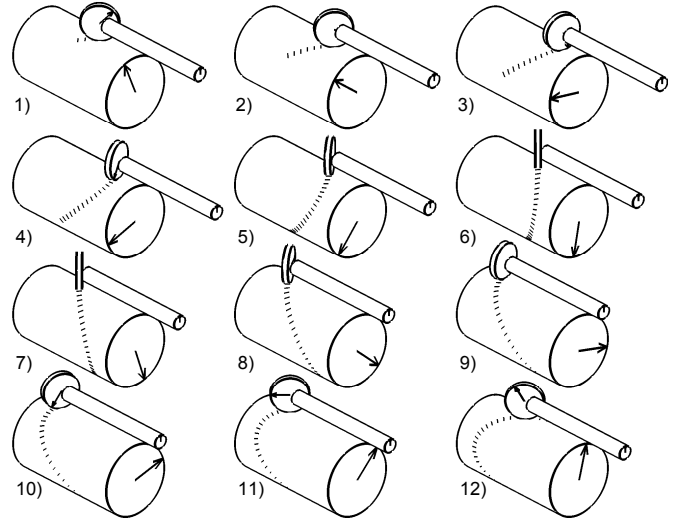

Fig. 1. A series of snapshots of the rotational-to-linear transmission as utilized to drive a prismatic link (tube) via a rotational input (cylinder). The transmission consists of a steered wheel pressed against a rotating cylinder, and travelling with a prismatic link.
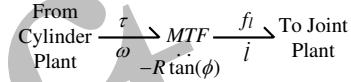

Fig. 2. A bond graph representation of the lossless rotational-to-linear transmission.

B. The Non-Ideal Rotational-to-Linear Transmission

In practice, the wheel and cylinder materials are not rigid bodies, and exhibit both elastic deformation and inelastic behaviors, leading to lateral creep losses and rolling losses. To elicit the kinematic equations that describe such a non-ideal transmission, we first diagram the relative velocities at the wheel-cylinder interface in wheel fixed frame $\hat{n}_1 - \hat{n}_2$ (see Figure 3). The wheel has radius, r, and rolling angular velocity, $\dot{\theta}$. The cylinder has radius, R, and angular velocity, ω. The prismatic link has linear velocity $\dot{l}$. The wheel has lateral creep velocity u, a flow loss of the transmission. Summing relative velocities at the wheel-cylinder interface in the $\hat{n}_1$ and $\hat{n}_2$ directions yields

$$u = \dot{l} \cos\phi + R\omega \sin\phi \tag{3}$$

and

$$r\dot{\theta} = \dot{l} \sin\phi - R\omega \cos\phi. \tag{4}$$

These equations describe geometric compatibility. In Figure 4 we diagram the forces acting at the wheel-cylinder interface in cylinder fixed frame $\hat{j}_1 - \hat{j}_2$. The cylinder has effort, τ, the prismatic link, f_l, the rolling wheel, $\tau_{in} + \tau_{wa}$, and the lateral creep effect results in effort, f_u. Summing forces at the wheel-cylinder interface in the $\hat{j}_1$ and $\hat{j}_2$ directions yields

$$\frac{\tau}{R} = \sin\phi f_u - \cos\phi \frac{\tau_{in} + \tau_{wa}}{r} \tag{5}$$

and

$$f_l = -\cos\phi f_u - \sin\phi \frac{\tau_{in} + \tau_{wa}}{r}. \tag{6}$$
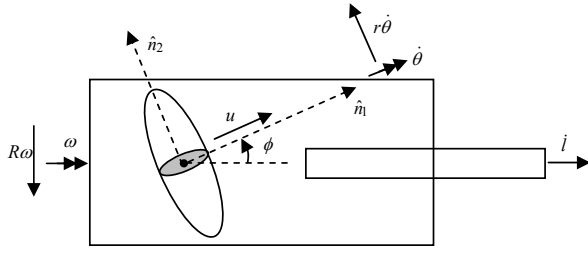
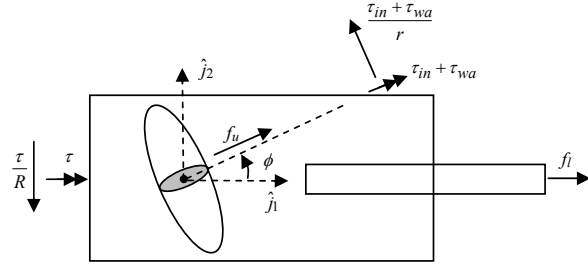Fig. 3. Velocity kinematics of the rotational-to-linear transmission, including flow loss due to lateral creep.

Fig. 4. Force balance of the rotational-to-liner transmission, including rolling losses due to inelastic materials, and wheel axle bearing friction. Note that f_l is defined as the force applied by the transmission to the link.

Torque, τ_{wa}, represents friction in the wheel axle and torque, τ_{in}, combats rolling friction (inelastic behavior) at the wheel-cylinder interface. These are rolling losses of the transmission.

Since the present analysis is for steady-state fixed steering angle operation of the rotational-to-linear transmission, two effects may be neglected. Steering friction torques are reacted by a steering motor (see [24] for a detailed depiction), and are not considered in the present analysis. In addition, since the tractive loads, τ_{in} and τ_{wa}, are small, and the present analysis is static (i.e rolling motion but no steering), kinematic creep is not present [19].

III. ANALYSIS OF THE COBOTIC TRANSMISSION

In this section we develop analytical models for lateral creep and rolling losses of the steady state rolling contact transmission, and incorporate these into a bond graph model. The models in this section accurately describe lateral creep and rolling losses of the rotational-to-linear transmission during steady-state operation only. Such conditions are characterized by a fixed transmission ratio and constant output effort and input flow. In general, no method except a full numerical method (not presented here) is applicable for analyzing dynamic rolling scenarios of elastic bodies where the rate of change of material strain is nonzero. In Section VI we do consider dynamic operation of the cobotic system as a whole, but do not present a set of models valid for dynamic operation of the rolling contact transmission since other system losses will dominate.

A. Lateral Creep Losses

A lateral creep loss, or deviation from the expected flow ratio given by Equation 1 is caused by the elastic deformation
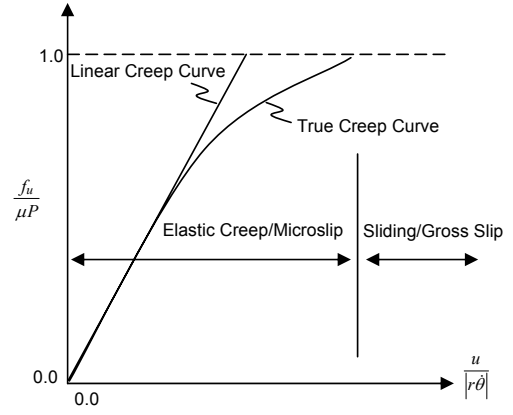

Fig. 5. Typical nondimensionalized lateral creep curve. This curve predicts lateral creep velocity, u, relative to forward rolling velocity, $r\dot{\theta}$, given the amount of lateral force applied to the wheel, f_u, relative to the force that will cause gross slip, μP. The true experimental creep curve is well approximated by a linear model up until 60-70 percent of μP.

properties of the wheel and the substrate it rolls on. Lateral creep is the ratio between lateral creep velocity, u, and rolling velocity, $|r\dot{\theta}|$, which results in lateral force, f_u (Figure 5). If we consider an elliptical patch between two elastic media with lateral and longitudinal halfwidths of length a and b, the *linear creep* model found in [14], [15], [25] may be employed to relate the lateral creep velocity to the lateral force,

$$f_u = -C_{22}Gab\frac{u}{|r\dot{\theta}|}. \tag{7}$$

The quantity $C_{22}Gab$ describes the material properties and geometry of the rolling contact and can be estimated or measured experimentally as shown below. The nondimensional creep coefficient, C_{22}, is a function of contact patch eccentricity and Poisson's ratio of the rolling bodies and is derived from a numerical model and tabulated by Kalker [15]. $G = (2(G_1^{-1} + G_2^{-1}))^{-1}$ is the combined shear modulus of elasticity for the two bodies in rolling contact. Contact patch halfwidths a and b may be estimated via Hertzian contact equations [14], [15].

The power dissipated by this deformation based effect,

$$\frac{\delta W_{def}}{dt} = uf_u = \frac{|r\dot{\theta}|}{C_{22}Gab}f_u^2, \tag{8}$$

is the product of the lateral creep velocity with the lateral force. This expression may be expanded in terms of flows of the transmission via Equation 4, and in terms of the cylinder or prismatic link effort via Equations 5 or 6, respectively.

If the wheel had significant tractive effort, longitudinal elastic creeps would also result, but we neglect these. The only tractive effort present is that required to combat friction in the bearing of the wheel axle, and no other power flows through this path.

The value of the material and geometry factor, $C_{22}Gab$, is experimentally characterized for the Cobotic Hand Controller in [26]. Consider a link commanded to have zero velocity, $\dot{l} = 0$, or equivalently, the rotational-to-linear transmission steered to $\phi = 0$. When a force f_l is then applied, the wheel

creeps laterally, resulting in link motion. The value

$$C_{22}Gab = -\frac{|r\dot{\theta}|}{u}f_u \approx -\frac{|R\omega|}{l}f_l \qquad (9)$$

can be derived from experiments which record flow, $\dot{l} \approx u$, in response to effort, $f_l \approx f_u$, and flow, $|R\omega| \approx |r\dot{\theta}|$ for $\phi = 0$. Other cobot literature characterizes this effect via *slip angles*, which describe the apparent angle at which the ideal transmission needs to be steered in order to produce the output flow given the output effort [19]. Slip angles or material geometry factor $C_{22}Gab$ are independent of cylinder speed.

B. Rolling Losses

The rolling contact also has two major sources of rolling losses, or deviations from the expected effort ratio given by Equation 2. These arise due to rolling friction at the contact patch of the transmission due to inelastic bodies, and friction in the wheel bearing[5] which sustains both the preload (radial) and lateral (axial) loads. Before any effort can be conveyed to the link, the cylinder must satisfy both the inelastic rolling friction and bearing friction.

1) Rolling friction: The inelastic compression and restitution of the wheel and cylinder as they roll together is known as free-rolling friction. The amount of strain work, δW_{strain}, done to the wheel and cylinder at the contact patch can be computed via a product of the distance rolled with an integral of the pressure distribution [14] as

$$\delta W_{strain} = d\theta \int_0^b p(y)y\,dy = \frac{2Pbd\theta}{3\pi}. \qquad (10)$$

We assume that we have two cylinders, loaded together via preload P, with a thin rectangular contact of longitudinal half-width b, with pressure distribution $p(y)$ in the longitudinal direction, where y is the coordinate in the $\hat{n}_2$ direction of Figure 3. We use the two cylinder assumption and rectangular contact patch approximation as this is particularly valid when $\phi \approx 0$ and inelastic losses (our present concern) are large relative to power throughput of the transmission and thus have a significant impact upon efficiency of the transmission. The energy dissipated to these inelastic hysteresis losses during free-rolling of a wheel, is a fraction,

$$\delta W_{in} = \alpha_{fr}\delta W_{strain}, \qquad (11)$$

of the strain energy. α_{fr} is a material dependent coefficient of restitution, called the hysteresis loss factor [14], which relates the expansive work regained to the compressive work spent. α_{fr} is not a constant for a given material, since it increases with strain (b/r) and varies with rolling history. In our case, strain is fixed due to the constant preload and to the steady-state rolling history, and a fixed value for α_{fr} can be utilized. Johnson [14] suggests that $\alpha_{fr} \leq 0.01$, or in other words, metals stressed within the elastic limit are at least 99 percent efficient at rolling.

---

[5]While the incorporation of the wheel bearing losses here may appear arbitrary, we endeavor to fit the transmission plant model into the format of Figure 10.

A rolling torque about the IVT wheel axis,

$$\tau_{in} = -\alpha_{fr}\mathrm{sgn}(\dot{\theta})\frac{2Pb}{3\pi}, \qquad (12)$$

can be computed that represents the effort required to keep the wheel rolling due to inelastic losses.

The power dissipated by the inelastic rolling is

$$\frac{\delta W_{in}}{dt} = -\tau_{in}\dot{\theta} = \alpha_{fr}|\dot{\theta}|\frac{2Pb}{3\pi}. \qquad (13)$$

$\frac{\delta W_{in}}{dt}$ is dependent on pre-load P but independent of transmission effort, f_l. Also note that $\frac{\delta W_{in}}{dt}$ is linear in input and output flows (if $\dot{\theta}$ is replaced via Equation 4), yielding a constant torque Coulombic effect rather than viscous behavior.

2) Wheel bearing friction: Bearings that sustain the radial preload on the IVT wheel, P, and the axial load, f_u, produce significant frictional dissipation. We utilize a *frictional moment and power loss* calculator provided by bearing manufacturer SKF [27] in order to determine the axle bearing friction portion of rolling friction torque on the IVT wheel, τ_{wa}. The resulting dissipated power is

$$\frac{\delta W_{wa}}{dt} = -\tau_{wa}\dot{\theta}. \qquad (14)$$

For our implementation, $\frac{\delta W_{wa}}{dt}$ is also Coulombic, but turns out to be 10 times larger than $\frac{\delta W_{in}}{dt}$. Like $\frac{\delta W_{in}}{dt}$, $\frac{\delta W_{wa}}{dt}$ is linear in cylinder speed. In [26] we examine SKF's calculator and show that τ_{wa} is dependent most significantly upon preload, P, and slightly on lateral force f_u, since the small coefficient of friction in our implementation ($\mu = 0.12$) requires that $P \gg f_u$.

3) Experimental characterization: The two effects cannot be individually isolated in our implementation of the Cobotic Hand Controller, but the power dissipated by the combination is easily isolated by measuring the change in cylinder motor torque with and without the wheels loaded against the cylinder [26]. The data confirms both that the models are of proper magnitude and that the effects are indeed predominantly Coulombic.

C. Bond Graph of Imperfect Transmission

The updated rolling contact transmission is characterized in Figure 6. The cylinder plant sources power $\tau\omega$. Effort is lost to rolling-friction losses at the contact patch, $\frac{\delta W_{in}}{dt}$, and to the IVT wheel axle bearing losses, $\frac{\delta W_{wa}}{dt}$. Flow loss, $\frac{\delta W_{def}}{dt}$, occurs due to elastic deformation based creep. The remaining power, $f_l\dot{l}$ flows to the link plant.

IV. STEADY-STATE EFFICIENCY OF ROTATIONAL-TO-LINEAR REDUCTION ELEMENT

In this section we evaluate the efficiency of the rotational-to-linear transmission for steady state operating conditions (i.e. in the absence of steering action). This is the efficiency of just the rolling contact element, and does not include losses of the link plant, cylinder plant, or steering plant, as these will be analyzed in a system level analysis in Sections V and VI.
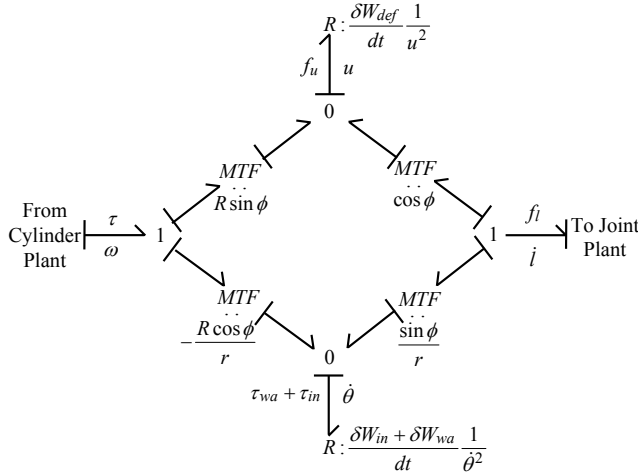
Fig. 6. Transmission plant portion of the cobotic transmission system. The modelled rolling losses, $\frac{\delta W_{in}}{dt}$ and $\frac{\delta W_{wa}}{dt}$, and lateral creep loss, $\frac{\delta W_{def}}{dt}$, have now been added to the lossless transmission plant introduced in Figure 2.

A. Theoretical Efficiency of the Reduction Element

The theoretical efficiency of the transmission, taking into account the modelled lateral creep and rolling losses, is simply power out divided by power in,

$$\eta_t = \frac{f_l \dot{l}}{\tau \omega}, \tag{15}$$

given a fixed steering angle, ϕ. Combining Equations 3 - 6, 7 and 15, provides six equations in eight unknowns, $(f_l, \dot{l}, \tau, \omega, \eta_t, f_u, u, \phi)$, allowing us to solve for

$$\eta_t(f_l, \phi) = -\frac{r \cos^2 \phi f_l (\sin \phi (h - k) + r f_l)}{(r \sin \phi f_l + h)(k \cos^2 \phi + r \sin \phi f_l + \sin^2 \phi h)}, \tag{16}$$

where $h = \tau_{in} + \tau_{wa}$ and $k = C_{22} Gabr$. The authors suggest modifying the computed efficiency to

$$\eta_t' = \eta_t \left(1 - \left(\frac{|f_u| - 0.7 \mu P}{0.3 \mu P} \right)^2 \right), \tag{17}$$

when $|f_u| = |\sec \phi f_l + \frac{h}{r} \tan \phi| > 0.7 \mu P$, in order to account for the nonlinear region of the lateral creep effect as shown in Figure 5.

B. Reduction Element Efficiency Experiment

We validate this theoretical model of reduction element efficiency by performing an experiment on a single transmission of the Cobotic Hand Controller. The experimental protocol to isolate the efficiency of the rolling contact reduction element is as follows: The steering plant fixes a transmission angle, ϕ, a priori. An approximate reduction ratio, $\frac{1}{\tan(\phi)}$, between cylinder surface speed, $R\omega$, and link speed, $\dot{l}$, is therefore set. The experimental efficiency of the rolling contact reduction element is defined as the mechanical power required to lift a known mass, m, via a pulley system, and to combat link guideway friction at constant velocity (both require power

flows through the reduction element), divided by the mechanical power provided to the reduction element via the product of cylinder torque and speed. The total mechanical power entering the reduction element (including that which is dissipated in the reduction element and that which flows through) is $\tau \omega = (\tau_{m,c} - \tau_{n,c}) n_c \omega$, the commanded motor torque less the nominal torque required to make the cylinder spin in the absence of any wheel loaded against it. n_c is the gear ratio between the cylinder motor and cylinder. Since the system is operating at a constant velocity, no mechanical power flows to the cylinder or carriage inertia and the steering plant is not in operation. The powers are integrated over time and computed as work done, which is useful since our linear and rotational sensors are position sensors. Thus the experimental efficiency of the reduction element is

$$\eta_e = \frac{(mg + c_l P \text{sgn}(\dot{l})) \int \dot{l} dt}{(\tau_{m,c} - \tau_{n,c}) n_c \int \omega dt}. \tag{18}$$

$c_l P \text{sgn}(\dot{l})$ is a Coulomb description of the link guideway friction force. P is determined via a known preload mechanism spring rate, c_l and $\tau_{n,c}$ are found experimentally, and m is measured via a mass balance. Motor torque, $\tau_{m,c}$, is commanded from a control loop that maintains ω, and is delivered by an amplifier in current mode. The motor/amplifier combination is calibrated with respect to the mass balance and with respect to a load cell used to determine the link output force, f_l.

Figure 7 displays the theoretical predictions of efficiency and the experimental efficiency data for the Cobotic Hand Controller's rolling contact reduction elements. The experiment and theoretical model is applied to a large range of transmission ratios, $\tan(\phi)$. The theoretical values of Equations 16 and 17 are plotted for five values of the ratio of link effort relative to preload force, $f_l/(\mu P)$, while the results of experimental efficiency, η_e, are provided at two values of this ratio. At 50 percent of peak output effort, $f_l/(\mu P) = 0.5$, the transmission is 50 percent efficient at 100:1 and 1:1 gear ratios, and 94 percent efficient near an 8:1 gear ratio.

C. Rolling-Contact Reduction Element Versus Gears

We compare the efficiencies of the cobotic transmission element to other types of gear trains in Figure 8. Planetary gear trains used for low torque applications, harmonic drives, and worm gears, have efficiencies similar to that of the cobotic rolling contact reduction element. However, while we report cobotic efficiencies at 15, 50 and 95 percent of peak power throughput, the efficiencies for gears are commonly reported at peak continuous power throughput where the predominantly Coulombic friction losses are smallest relative to the power throughput. Thus, in Figure 8, the cobotic reduction element may seem less efficient at low power throughput (the $\frac{f_l}{\mu P} = 0.15$ condition), relative to gears than it really is.

V. SYSTEM DESCRIPTIONS

Now that we have a model of the cobotic transmission element, we are in a position to compare the efficiency of a cobotic system to that of a conventional system, both tasked to
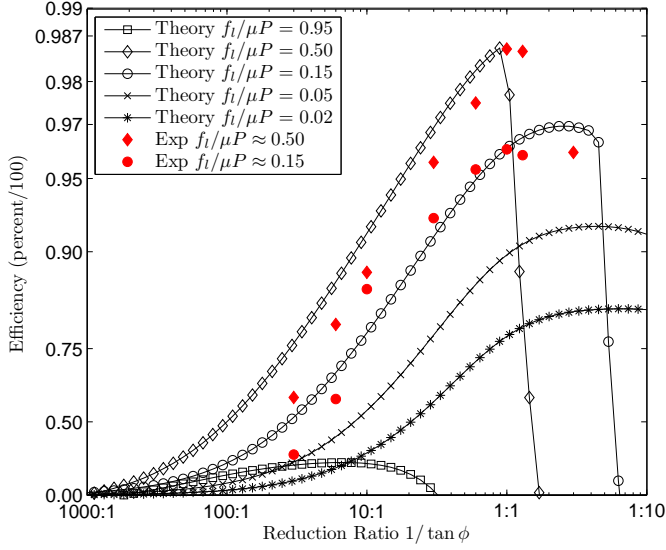
Fig. 7. Theoretical and experimental efficiencies of the rolling contact reduction element of the cobotic transmission, operating at various transmission ratios and levels of maximum effort. Experimental efficiencies are not reported for reduction ratios larger than 100 : 1, since accurate measurements become a difficulty, although the device is capable of rendering ∞ : 1 ratios, or a completely clutched state. We are also unable to experiment with the highest possible loading condition, $f_l/(\mu P) = 0.95$, due to the unpredictable nature of friction near the breakaway force.
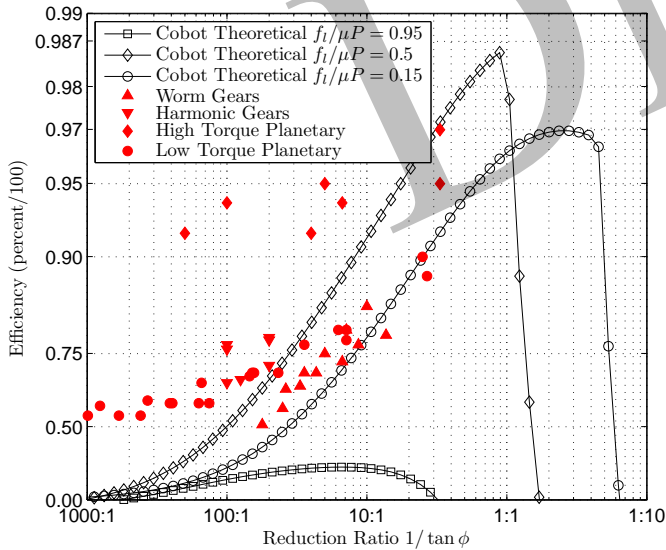

Fig. 8. Efficiency of the rotational-to-linear rolling contact reduction element versus conventional gears sampled at random from the Internet. Only very expensive, very high torque planetary gear trains (not useful for low power applications in the proximity of human operators), or single gear pairs can achieve efficiencies above 90 percent. The cobotic efficiencies are reported for various percentages of maximum effort throughput, $f_l/(\mu P)$, at a given flow ratio, $1/\tan(\phi)$. The cobotic efficiencies fall off steeply at large reduction (flow) ratios as rolling friction losses become large relative to power throughput.
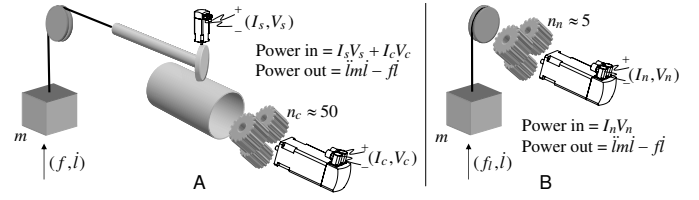

Fig. 9. A. Cobotic architecture. B. Conventional architecture. The output for each drive-train is the flow, $\dot{l}$, of the mass, m. The conventional system requires electrical power, $I_n V_n$, while the cobotic system requires steering power, $I_s V_s$, and cylinder power, $I_c V_c$. Both systems allow an external force, f, to apply effort to the load.
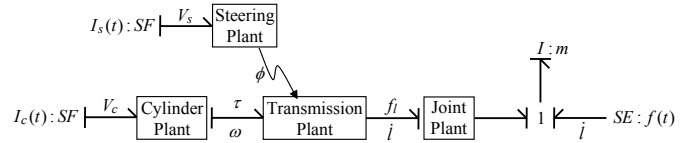

Fig. 10. A general cobotic system is composed of four plants detailed in Figures 11 through 13. The plants allow two current sources and a human effort source to do work on a mass, m. The steering plant adjusts the modulus of the transformer in the transmission plant, but no power flows between the steering plant and transmission.
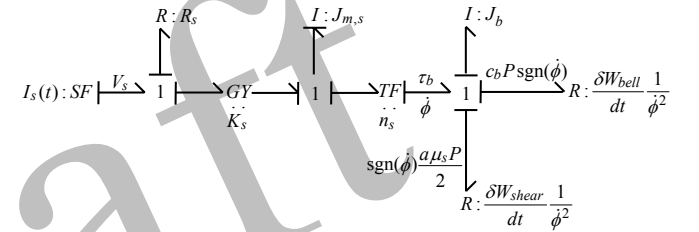

Fig. 11. The steering plant portion of the cobotic system converts electrical power into the angle ϕ, the modulus of the transformer in the cobotic transmission. Losses include Ohmic heating, dissipation at the contact patch ($\frac{\delta W_{shear}}{dt}$) and bell bearing ($\frac{\delta W_{bell}}{dt}$), both of which sustain preload P, and power required to drive inertia of the steering motor ($J_{m,s}$) and housing of the wheel (J_b). We ignore any losses in the small gear reduction n_s.

meet the same requirements. This section develops bond graph descriptions of cobotic and conventional systems as iconically depicted in Figure 9. We define a conventional system as a rotational electrical motor coupled through a fixed-ratio gear-train, to a pulley or capstan drive, in order to impose a straight line velocity on a mass, m. While the conventional drive-train requires a single motor, we will compare this to the combined power of the driving and steering motors in the rotational-to-linear cobotic system.

A. Cobotic System Description

Figure 10 depicts a bond graph describing a cobotic system, including a rotational-to-linear transmission, steering, cylinder and link plants. No controller elements are shown on this graph, only electrical and physical elements. The inputs to the bond graph are steering and cylinder motor currents I_s and I_c along with interaction force f. The output is the resulting motion of mass, m. Load m is in addition to the nominal link mass, m_l, depicted in the joint plant of Figure 13.

1) Steering plant: Moving from left to right in the steering plant (Figure 11), we see electrical current, I_s, gyrator, K_s,

and Ohmic heating in motor resistance, R_s. Once the gyrator creates rotational power, effort flows into the inertia of the steering motor, $J_{m,s}$ and to the transformer, n_s, representing gearing between the steering motor and the bell that contains the IVT wheel. This is followed by the final 1-junction, driving the steering bell inertia, J_b, the dissipation of the bell bearing, $\frac{\delta W_{bell}}{dt}$, and the dissipation of the contact patch, $\frac{\delta W_{shear}}{dt}$. Steering action causes shear dissipation, $\frac{\delta W_{shear}}{dt} = \mathrm{abs}(\dot{\phi})\frac{a\mu_s P}{2}$, at the contact patch, assuming a relatively uniform pressure distribution along a line contact. μ_s is a dynamic sliding coefficient of friction, different from the rolling coefficient of friction, μ. The steering bell bearing dissipation, $\frac{\delta W_{bell}}{dt}$ can be represented by a Coulombic model, $c_b P \mathrm{sgn}(\dot{\phi})$, where a dynamic coefficient of Coulombic bell friction c_b is denoted.

2) Cylinder plant: Moving from left to right in the cylinder plant (Figure 12), we see electrical current, I_c, driving gyrator, K_c, and Ohmic heating in motor resistance, R_c. After the gyrator power flows to the inertia of the cylinder motor, $J_{m,c}$, to the transformer, n_c (gearing between the cylinder motor and cylinder), and to any dissipation of this transformer and cylinder bearings, $\frac{\delta W_{nominal}}{dt}$. The effort of this transformer drives the cylinder inertia, J_c, and provides torque, τ, to the transmission plant at cylinder velocity, ω. We do not model any compliance in the cylinder or steering plant gear-trains. Although this compliance could significantly impact controller dynamics, it will not dissipate significant energy so as to affect the present analysis of efficiency and power consumption.

3) Joint plant: Translational power $f_l \dot{l}$ flows into the link plant depicted in Figure 13. This plant consists of a common flow junction that distributes power to the external loads, the link inertia, m_l, and to power dissipated by link guideway friction, $\frac{\delta W_{lg}}{dt}$.

B. Conventional System Description

The bond graph of our hypothetical *conventional* electro-mechanical plant is depicted in Figure 14. Moving from left to right, the junctions represent power flow to the electrical resistance of the motor, the conversion of electrical power to mechanical power, the inertia of the motor, a single stage gear reduction, n_n, friction and inertia due to gears, pulleys and cables in the system and, finally, the pulley radius transformer, r_{pulley}, that converts rotation to translation.

VI. COMPARATIVE ANALYSIS OF SYSTEM EFFICIENCIES

In order to develop a fair comparison between the power efficiency of conventional and cobotic systems, we first define a common set of design goals. These goals are a desired operating regime in the force, f_l, versus velocity, $\dot{l}$, plane. A designer of a linear actuation system will likely specify a maximum force required, a maximum velocity required and also a maximum power that is expected at any given time. An area in the force-velocity plane is then developed from these three specifications as illustrated by the darkest shaded area in Figures 15 and 16. Given the desired operating regime for steady-state power flows (constant velocity and constant force), conventional and cobotic systems are designed and evaluated in Sections VI-A and VI-B respectively.
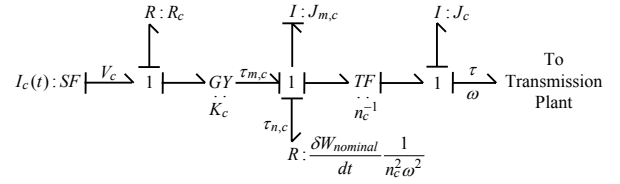

Fig. 12. The cylinder plant portion of the cobotic system converts electrical power into mechanical power $\tau\omega$. Power is lost to Ohmic heating, friction in the cylinder bearings and gear-train ($\frac{\delta W_{nominal}}{dt}$), and to the cylinder motor and cylinder inertias, $J_{m,c}$ and J_c respectively.

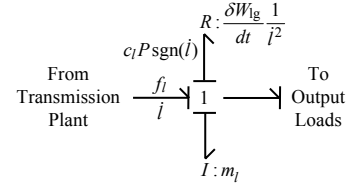Fig. 13. The link plant portion of the cobotic system. Power is lost to friction in the link, $\frac{\delta W_{lg}}{dt}$, and to accelerate the mass of the link, m_l, before any external load can be driven.
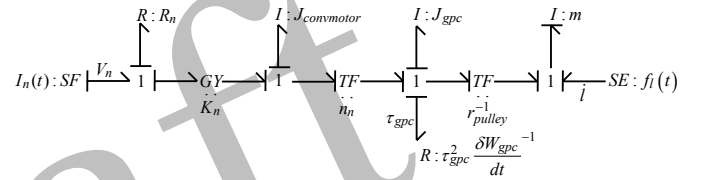

Fig. 14. A conventional fixed-ratio rotary-electric to linear system as depicted in Figure 9. Power is lost to Ohmic heating, friction in the gear-train and cabling $\frac{\delta W_{gpc}}{dt}$, and to the inertia of the motor, gearing, pulley and cable, J_{gpc}, before power can be transmitted to external loads.

A. Analysis of Conventional System Steady-State Efficiency

We evaluate the efficiency and feasible operating regime in the force-velocity plane for four conventional power-train designs of the framework outlined in Figure 14. The goal of this analysis is to determine the smallest motor with which the conventional architecture can meet the maximum force, maximum velocity and maximum power specifications. A series of hypothetical systems, with the architecture outlined in Figure 14, are designed to meet these specifications. A Matlab simulation evaluates the feasible operating regimes and power efficiencies. Efficiency is evaluated as mechanical power out divided by electrical power in: $|\frac{\ddot{l}m\dot{l}-f\dot{l}}{I_n V_n}|$. This simplifies to $|\frac{-f\dot{l}}{I_n V_n}|$, given that $\ddot{l} = 0$ for a steady-state power flow scenario. Losses include Ohmic heating of the motor windings and friction of the gear-train, pulley and cable. No power flows into inertial components when operating at constant force and constant velocity.

The feasible operating regime is limited by the maximum continuous torque of the motor and the maximum velocity of the motor. Motor 1 has the properties of a Maxon^{TM} Re-max 29 brushed DC motor (22 watt, Maxon num. 226806) and Motor 2 is a version of this scaled up in strength (and weight and power consumption, etc.) by a factor of 2.7. Both have
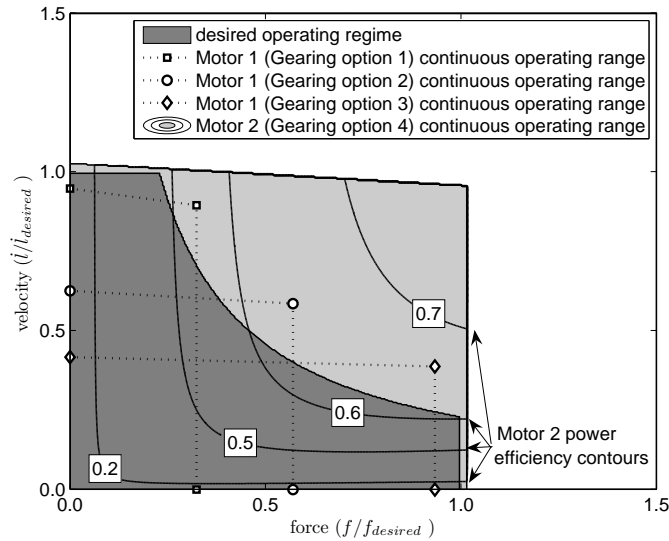
Fig. 15. The ranges of operation of some conventional drive-train designs, and contours of power efficiency of the Motor 2 design. The darker shaded region indicates the desired operating regime, and the lighter shaded region is the continuous operating regime of Motor 2. $\dot{l}_{desired}$ and $f_{desired}$ are the desired maximum velocity and force specifications. Motor 2 is 2.7 times larger than Motor 1.
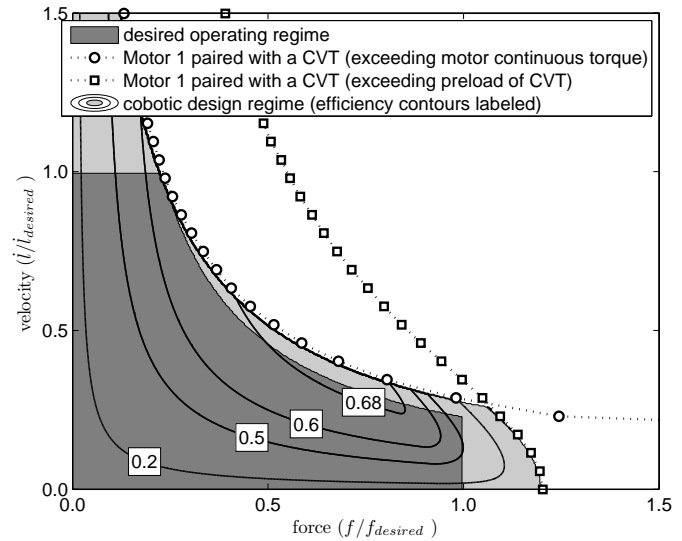

Fig. 16. The range of operation of a cobotic drive-train using the same Motor 1 as the conventional drive-train design in Figure 15. The feasible cobotic design regime (indicated by the lighter shaded region) is bounded where the required effort would cause the IVT wheel to slip, and where the required motor torque exceeds the motor's thermal limit. $\dot{l}_{desired}$ and $f_{desired}$ are the desired maximum velocity and force specifications.

peak efficiencies of 87 percent. The four gearing options are all single stage planetary gear-heads with efficiency of 97 percent. Gear efficiencies are implemented in the simulation by adding a Coulombic friction torque of $\tau_{coulombic} = (1 - \eta)\tau_{cont}$, where eta is the gear efficiency at continuous rated torque, τ_{cont}.

In Figure 15 we show the performance capabilities of various conventional electro-mechanical drive-train designs (Motor 1 with Gearing 1, Motor 1 with Gearing 2, Motor 1 with Gearing 3 and Motor 2 with Gearing 4).

Although Motor 1 is paired with several different gear ratios, it cannot achieve the maximum force and maximum velocity specifications simultaneously. It has no trouble developing the required power specification, but cannot do so across the range of operating conditions. The right hand boundary of the continuous operating regimes is limited by the continuous torque that a motor can develop without overheating.[6] In order to achieve the maximum force and velocity specifications for a single gear ratio, a much larger Motor 2 must be selected, which has more power capability than will ever be needed. Motor 2's continuous operating regime is shown by the lighter shaded area in Figure 15, and will be compared with the lighter shaded region in Figure 16. Given that Motor 2's power capability is larger than needed, it never operates at maximum power, and therefore does not operate at high efficiency.[7] Much of the electrical power is lost to resistive heating of the motor windings as it operates at inefficient speeds. Although the combination of Motor 2 and the Gearing 4 is capable of 85

[6]The sloping upper boundary is the motor's maximum velocity given the operating voltage and applied torque. This sloping boundary would intersect the horizontal axis at the momentary stall torque achievable by the motor.

[7]Maxon provides a useful reference for motor dynamics at http://www.maxonmotorusa.com/media/maxontechnology/02_selandcal_e.pdf. [28].

percent power efficiency, it never exceeds 65 percent efficiency in our desired operating regime (note the efficiency contours for Motor 2 in Figure 15).

B. Analysis of Cobotic System Steady-State Efficiency

We evaluate the efficiency and feasible operating regime in the force-velocity plane of a single leg of the Cobotic Hand Controller system as outlined in Figure 10. In a steady-state analysis of the cobotic drive-train, we are concerned with the efficiency of the transmission plant in the absence of any steering action. Thus a steering angle has been set and no electrical flow is required in order to maintain the angle of the IVT. Efficiency is evaluated as mechanical power out divided by electrical power in: $|\frac{\ddot{l}m\dot{l} - f\dot{l}}{I_s V_s + I_c V_c}|$. This simplifies to $|\frac{-f\dot{l}}{I_c V_c}|$, given that $\ddot{l} = 0$ and $I_c = 0$ for a steady-state power flow scenario. Losses consist of elastic deformation based creeps and inelastic rolling friction, Ohmic heating and frictional losses of the cylinder motor, frictional losses of the gear-set driving the cylinder, and friction of the linear guideway. No power flows into the inertias of the system since we are holding the velocity constant. Likewise, no power flows to the steering plant since the angle is fixed for this scenario.

The feasible bounds of operation in the force velocity range are also computed. They are limited both by maximum cylinder motor torque and available friction force (preload). They are not limited by cylinder motor speed, since we use a fixed-speed cylinder controller set to $\omega = 14$ rads/s, and the cylinder motor is operating at its most efficient speed of 8040 RPM, through a gear ratio of $n_c = 57 : 1$. The gear-train, n_c, has a maximum efficiency of 88 percent, possible for a high end harmonic drive, or a high-torque planetary gear-set.

A Matlab simulation evaluates the feasible operating regime and power efficiency. Figure 16 displays steady-state efficiency

predictions of the cobotic system defined in Figure 10. The velocity limit of Motor 1 is not an issue for the cobotic system since it is operating constantly at its most efficient speed. The smaller Motor 1, although insufficient to meet our performance criteria in the conventional drive-train, is sufficient in the cobotic drive-train design. The cobotic drive-train's infinitely variable transmission allows the capture of maximum power of Motor 1 across all forces and velocities. In addition, higher power efficiencies are reached by the cobotic drive-train than the conventional drive-train at any given point, since the cobotic drive-train's motor is always operating at an efficient speed. Nevertheless, the significant gear reduction between the cylinder motor and cylinder limits the cobotic drive-train's efficiency to somewhat less than 75 percent (the product of 88 percent gearing efficiency and an 87 percent efficient motor and a 98 percent efficient rolling contact, which are not necessarily simultaneously maximal).

C. Analysis of Dynamic System Performance

We evaluate the performance and feasible operating regimes of the cobotic and conventional systems for the task of shaking mass m at various frequencies and amplitudes. This scenario will require additional power to steer the wheel or modulate the transmission of the cobotic system, and to accelerate and decelerate inertias in each system.

The space of dynamic operating conditions will be characterized by frequency, ϖ, and by a percentage of maximum power throughput. The maximum power throughput is the steady-state maximum power specification from Figures 15 and 16. We now consider this continuous power an RMS power, $\frac{\delta W_{RMS}}{dt}$. We evaluate the amplitude of l, α, at which m must be shaken in order to achieve this power. An amplitude of motion, $\alpha = \sqrt{\frac{2\sqrt{2}}{m\varpi^3}\frac{\delta W_{RMS}}{dt}}$ m/s, is computed.[8] Each system is worked through one cycle of this motion and the desired power is divided by the electrical power requirements to yield the dynamic performance of the systems. Performance is computed as $\int |\frac{\ddot{l}ml}{I_n V_n}|dt$ for the conventional system and as $\int |\frac{\ddot{l}ml}{I_s V_s + I_c V_c}|dt$ for the cobotic system. No external forces f are present for this scenario. We assume that the cylinder is driven at constant speed. Again, Matlab simulations for the systems depicted in 10 and 14 are used to evaluate the feasible operating regimes and performance.

Figure 17 depicts a comparison of the conventional and cobotic system performance across a range of frequencies and across a range of fraction of maximum specified power throughput.

The cobotic system can achieve quite high dynamic performance compared to the conventional system, as it adjusts the transmission ratio so that the motor need not apply large torques when the mechanical power requirements are low; exactly the situation that leads to resistive heating losses for the conventional system that are high relative to mechanical power throughput. The reason that performance is as high as 85 percent for the cobotic drive train, is that the motor amplifier

---

[8]The RMS power is evaluated from instantaneous power, $\dot{W}(t) = \ddot{l}(t)m\dot{l}(t) = m\alpha^2\varpi^3\sin(\varpi t)\cos(\varpi t)$.
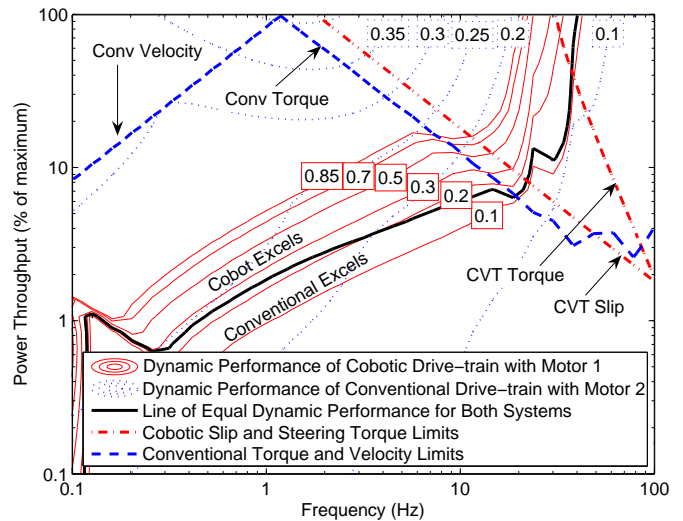

Fig. 17. Comparison of the power efficiency contours of cobotic drive-trains and conventional drive-trains at driving a mass sinusoidally. Neither system can work in the upper right portion of the plot and only the cobotic system can work in the upper left portion.

must only source electrical power when it needs to do work on the load. Otherwise - we assume that a decelerating load does work on a regenerative resistor provided the inertial torque is greater than the frictional torque. If we instead assumed that this energy could be completely recouped via a battery or capacitor, the electrical power requirements would be even less - and our measure of performance even higher - as only frictional power requirements (not inertial) would be still be relevant.

The analysis here compares our best attempts at designing two different architecture systems to meet the same specifications. While the results are certainly not quantitatively precise, they have important qualitative implications. In general, Figure 17 portrays the cobotic drive-train as having higher power throughput than the conventional drive-train at less than 10 Hertz and greater than 10 percent of the maximum power throughput. In this regime, the cobot is losing the majority of its power to the steering plant, and the conventional drive-train is losing most of its power to electrical resistance. At the mid-range frequencies of voluntary human motion (one to ten hertz), the two drive-train types have relatively similar power efficiencies, even with the additional expenditure of modulating the steering angle by the cobot. Both systems show increasing efficiency with increasing power throughput since many of their losses are due to Coulombic friction or Ohmic heating of motor windings. Both systems also exhibit decreasing performance at high frequencies since, in addition to accelerating the load, inertias in the drive-trains must also be accelerated.

There is much room for improvement of the dynamic performance in our current cobotic design. This can be accomplished by reducing the rotational inertia of the steering plant, and by reducing the mass of the linearly moving link plant.

VII. CONCLUSION

We have provided a thorough analysis of the rotational-to-linear cobotic transmission, describing all forms of dissipative losses at the contact patch and in the remainder of the cobotic architecture. The modelling of dissipative losses can help us define key material parameters for cobot transmission design. The free-rolling friction coefficient, α_{fr}, should be minimized in order to reduce inelastic losses. The utilization of steel-on-steel and the resulting high preloads described here may have been too extreme since the IVT wheel axle bearings are a source of dissipation on the order of ten times larger than the inelastic rolling friction at the contact patch, although steering torque is reduced and transmission stiffness increased. Increasing the modulus of elasticity, G, would reduce lateral creep. Increasing the coefficient of friction, μ, reduces the required preload, and consequently reduces nearly all forms of dissipation, with the exception of lateral creep. Reducing bearing diameters, specifically the steering bell and IVT wheel axle bearings, may significantly reduce frictional power dissipation. Finally, increasing the specific strength of materials for the cylinder, bell, and carriage would reduce inertial losses. The relative impact of these parameter changes has been provided for the rotational-to-linear IVTs of the Cobotic Hand Controller [26]. The benefits of utilizing a traction fluid to reduce component wear, while not decreasing the coefficient of friction, have been left out of this work which focuses on dry-friction.

Given a set of design criteria for a multi-degree-of-freedom mechanism, such as maximum flow, maximum effort and maximum power, we find that a cobot can meet these requirements with reduced numbers of high power actuators, reduced size requirements for those actuators and increased power efficiency relative to conventional actuation systems for frequencies of voluntary human motion. We envision power efficient cobots as an enabling technology for haptics and prosthetics that will allow for increases in the dynamic range of these devices while simultaneously permitting reductions in actuator size and power requirements. Use of an IVT eliminates the need to make compromises on flow and effort, which are inherent to choosing a fixed transmission ratio. The result is mechanisms with enhanced dynamic range that extends infinitely from a completely clutched state to a highly backdrivable state.

REFERENCES

[1] J. Colgate and M. Peshkin, "U.S. Patent No. 5952796: Cobots," Patent, September, 1999.

[2] M. Peshkin, J. Colgate, W. Wannasuphoprasit, C. Moore, R. Gillespie, and P. Akella, "Cobot architecture," *IEEE Transactions on Robotics and Automation*, vol. 17, no. 4, pp. 377–390, 2001.

[3] R. Gillespie, J. Colgate, and M. Peshkin, "A general framework for cobot control," *IEEE Transactions on Robotics and Automation*, vol. 17, no. 4, pp. 391–401, 2001.

[4] C. Moore, M. Peshkin, and J. Colgate, "Cobot implementation of virtual paths and 3D virtual surfaces," *IEEE Transactions on Robotics and Automation*, vol. 19, no. 2, pp. 347–351, 2003.

[5] W. Wannasuphoprasit, R. Gillespie, J. Colgate, and M. Peshkin, "Cobot control," in *International Conference on Robotics and Automation*, Albuquerque, NM, 1997, pp. 3571–3576.

[6] C. Hunt, "U.S. Patent No. 197472: Counter-shaft for driving machinery," Patent, 1877.

[7] R. Fuchs, Y. Hasuda, and I. James, "Dynamic performance analysis of a full toroidal IVT: A theoretical approach," in *International Continuously Variable and Hybrid Transmission Congress*, 2004.

[8] J. Newall, S. Cowperthwaite, M. Hough, and A. Lee, "Efficiency modelling in the full toroidal variator: Investigation into optimization of EHL contact conditions to maximize contact efficiency," in *International Continuously Variable and Hybrid Transmission Congress*, 2004.

[9] H. Machida and Y. Murakami, "Development of the POWERTOROS UNIT half toroidal CVT," *NSK Technical Journal Motion and Control*, no. 9, pp. 15–26, 2000.

[10] B. Pohl, M. Simister, R. Smithson, and D. Miller, "Configuration analysis of a spherical traction drive CVT/IVT," in *International Continuously Variable and Hybrid Transmission Congress*, 2004.

[11] P. Milner, "U.S. Patent No. 6461268: Continuously variable transmission device," Patent, 2002.

[12] Y. Nakamura, W. Chung, and O. Sordalen, "Design and control of the nonholonomic manipulator," *IEEE Transactions on Robotics and Automation*, vol. 17, no. 1, pp. 48–59, 2001.

[13] J. Kim, F. Park, Y. Park, and M. Shizuo, "Design and analysis of a spherical continuously variable transmission," *Journal of Mechanical Design*, vol. 124, no. 1, pp. 21–29, 2002.

[14] K. Johnson, *Contact mechanics*. Cambridge, U.K.: Cambridge University Press, 1985.

[15] J. Kalker, *Three-dimensional elastic bodies in rolling contact*. Dordrecht, Boston: Kluwer Academic Publishers, 1990.

[16] C. Moore, "Continuously variable transmission for serial link cobot architectures," Masters Thesis, Northwestern University, 1997.

[17] L. Jabre, R. McGrew, R. Gillespie, and P. Goleski, "An assistive cobot for aid in self-care activities," in *IFAC Conference on Mechatronic Systems*, 2002.

[18] G. Bachman, "An experimental investigation of the cobot wheel contact patch," Masters Thesis, Northwestern University, 1997.

[19] R. Gillespie, C. Moore, M. Peshkin, and J. Colgate, "Kinematic creep in continuously variable transmissions: Traction drive mechanics for cobots," *Journal of Mechanical Design*, vol. 124, no. 4, pp. 713–722, 2002.

[20] M. Brokowski, "Experimental characterization of a spherical continuously variable transmission," Ph.D. Dissertation, Northwestern University, 2002.

[21] M. Brokowski, S. Kim, J. E. Colgate, R. Gillespie, and M. A. Peshkin, "Toward improved CVTs: Theoretical and experimental results," in *ASME IMECE DSC*, New Orleans, LA, 2002.

[22] S. Kim, "Control of the powered arm cobot and analysis of the rotational CVT," Ph.D. Dissertation, Northwestern University, 2003.

[23] D. Karnopp, D. Margolis, and R. Rosenberg, *System Dynamics*. New York, NY: John Wiley & Sons, Inc., 2000.

[24] E. Faulring, J. Colgate, and M. Peshkin, "A high performance 6-DOF haptic cobot," in *IEEE International Conference on Robotics and Automation*, New Orleans, LA, 2004, pp. 1980–1985.

[25] P. Vermeulen and K. Johnson, "Contact of non-spherical elastic bodies transmitting tangential forces," *Journal of Applied Mechanics*, vol. 31, pp. 338–340, 1964.

[26] E. Faulring, "The cobotic hand controller: Design, control and analysis of a novel haptic display," Ph.D. Dissertation, Northwestern University, 2005.

[27] SKF, "Frictional moment - power loss calculations," October 2005, http://www.skf.com/portal/skf/home/products?maincatalogue=1&newlink=first&lang=en.

[28] Maxon Precision Motors Inc., "Key information on Maxon DC motor and Maxon EC motor," August 2006, http://www.maxonmotorusa.com/media/maxontechnology/02_selandcal_e.pdf.